Chemical Science

ROYAL SOCIETY OF CHEMISTRY

EDGE ARTICLE

View Article Online
View Journal | View Issue

Cite this: *Chem. Sci.*, 2026, **17**, 5103

All publication charges for this article have been paid for by the Royal Society of Chemistry

The relevance of Cr defects and photoelectrochemical water oxidation activity of monoclinic $PbCrO_4$ films

Jiahe Li,[a] Gaili Ke,[a] Minji Yang,[b] Guoliang Lv,[a] Lanyi Cao,[a] Wenjun Li,[a] Tao Han,[a] Wenrong Wang,[a] Yong Zhou[c] and Huichao He*[a]

The presence of Cr defects in monoclinic $PbCrO_4$ is closely related to its solar water oxidation activity, which has been overlooked in the preparation of $PbCrO_4$ films and remains unexplored in research on $PbCrO_4$ photoanodes. Herein, monoclinic $PbCrO_4$ films with few Cr defects ($PbCrO_4$-$F_{V_{Cr}}$) were prepared on FTO substrate by drop-coating Pb^{2+}/Cr^{3+} precursor solution to reduce the loss of Cr during thermal treatment. Relative to the monoclinic $PbCrO_4$ films with rich Cr defects ($PbCrO_4$-$R_{V_{Cr}}$), higher solar water oxidation activity was achieved using the $PbCrO_4$-$F_{V_{Cr}}$ films as photoanodes. At 1.23 V *vs.* RHE, a higher water oxidation photocurrent of 1.13 mA cm^{-2} was produced on the $PbCrO_4$-$F_{V_{Cr}}$ film photoanodes, which is twice that of the $PbCrO_4$-$R_{V_{Cr}}$ film photoanodes (0.55 mA cm^{-2}). Meanwhile, the $PbCrO_4$-$F_{V_{Cr}}$ film photoanodes had faster water oxidation kinetics than $PbCrO_4$-$R_{V_{Cr}}$ film photoanodes. The water oxidation rate constant (k_{O_2}) on the $PbCrO_4$-$F_{V_{Cr}}$ film photoanodes was 40.6 s^{-1}, while a lower k_{O_2} of 8.2 s^{-1} was observed on the $PbCrO_4$-$R_{V_{Cr}}$ film photoanodes. Experimental and theoretical analyses jointly revealed that $PbCrO_4$ films with fewer Cr defects have higher solar water oxidation activity for the following reasons: (i) the presence of Cr defects can result in the formation of deep energy levels in $PbCrO_4$, which are unfavorable for carrier transfer in the bulk of $PbCrO_4$ films; (ii) the presence of Cr defects leads to the formation of unsaturated O dangling bonds on $PbCrO_4$, which act as detrimental traps that hinder carrier separation at the surface of $PbCrO_4$ films; (iii) Cr has a half-filled $3d^5$ orbital to provide active sites for reaction, so the presence of Cr defects weakens the catalytic activity of $PbCrO_4$ for water oxidation, and the dehydrogenation of *OH into *O becomes the rate-limiting step, which requires a high energy barrier of 1.88 eV. The present work provides insights into monoclinic $PbCrO_4$ film photoanodes in terms of preparation conditions, Cr defects, water oxidation activity and reaction mechanism.

Received 4th November 2025
Accepted 1st January 2026

DOI: 10.1039/d5sc08541a

rsc.li/chemical-science

1 Introduction

n-Type monoclinic $PbCrO_4$ has an electronic structure similar to that of monoclinic $BiVO_4$,[1] and it has been investigated as a photoanode material for photoelectrochemical (PEC) water splitting in recent years.[2–7] Based on its advantageous band gap (~2.2 eV) and valence band position (~2.2 V *vs.* RHE),[2] monoclinic $PbCrO_4$ can theoretically harvest ~20% of solar energy to drive water oxidation.[8] However, the activity of previously reported $PbCrO_4$ photoanodes is far below the theoretical expectation, due to the presence of high carrier recombination and sluggish water oxidation kinetics. As is well known, the composition and structure of materials jointly determine their properties and related performance. The presence of defects in semiconductors could impact their electronic structure, carrier separation and migration behavior, thereby obviously changing the photocatalytic and PEC activity.[9,10] For monoclinic $PbCrO_4$, its Cr^{6+} is located at the center of a CrO_4 tetrahedron, and Pb^{2+} is surrounded by 8–9 oxygen atoms due to its lone pair electron effect.[11,12] From the perspectives of electronic structure, one Cr defect carries three effective negative charges ($V_{Cr}^{'''}$) in $PbCrO_4$. In theory, the presence of a high concentration of Cr defects could disrupt the CrO_4 tetrahedron network and form unsaturated O dangling bonds as well as defect-level traps, which are disadvantageous to the delocalized separation and transfer of electrons/holes.

Significantly, drop-/spin-coating combined with thermal treatment is a common approach for the preparation of monoclinic $PbCrO_4$ film. Typically, Li *et al.* used a spin-coating/thermal treatment method to prepare $PbCrO_4$ films on fluorine-doped tin oxide-coated glass (FTO), and invented acetylacetone

[a]*College of Materials and New Energy, Chongqing University of Science and Technology, Chongqing 401331, China. E-mail: hehuichao@cqust.edu.cn*

[b]*Synthetic Lubricant Oil and Grease Branch, Sinopec Lubricant Co., Ltd, Chongqing, 400039, China*

[c]*Ecomaterials and Renewable Energy Research Center, School of Physics, University Nanjing, Nanjing 211102, China*

and poly(ethylene glycol) as dual ligands to regulate the nucleation and crystal growth of monoclinic $PbCrO_4$ films.[4,6] Cho *et al.* prepared $PbCrO_4$ films on FTO using a drop-coating/thermal treatment approach, and found that adding citric acid to the precursor solution can stabilize Pb^{2+} and Cr^{3+} as well as suppress their segregation to form a smooth and fine monoclinic $PbCrO_4$ film.[5,7] Although these pioneering investigations made significant contributions to the preparation of monoclinic $PbCrO_4$ films, the underlying influence of thermal treatment on the composition and structure of the resultant $PbCrO_4$ films has been overlooked. During thermal treatment at high temperature in air, the metal ions in the precursor solution may be lost, along with the pyrolysis of solvents, which could induce the formation of metal defects in the resultant multi-metal oxides. In the preparation of $BiVO_4$ films using a spray pyrolysis method, Lamers *et al.* found the loss of V during the VO^{3+}/Bi^{3+} precursor solution annealing above 500 °C in air, and observed that the resultant $BiVO_4$ films contained V defects and low carrier mobility.[13] It is worthy of special attention that Cr can be thermally evaporated at lower temperature (T > 500 °C) compared to Pb (T > 600 °C). The thermal evaporation of Cr from stainless steels at T > 500 °C has been extensively observed.[14] Thus, it is very possible that Cr defects are formed in monoclinic $PbCrO_4$ films prepared using drop-/spin-coating combined with thermal treatment for synthesis. Several works have demonstrated that semiconductor photoelectrode materials with low-concentration defects usually have high crystallinity and can drive solar water splitting efficiently.[15–17] To achieve efficient solar water oxidation on $PbCrO_4$ film photoanodes, suppressing the formation of high concentrations of Cr defects in monoclinic $PbCrO_4$ films during synthesis is crucial.

Herein, monoclinic $PbCrO_4$ films with few Cr defects ($PbCrO_4$-$F_{V_{Cr}}$) were prepared on FTO substrate by drop-coating the Pb^{2+}/Cr^{3+} precursor solution to reduce the thermal loss of Cr during annealing treatment. Compared with the monoclinic $PbCrO_4$ films with rich Cr defects ($PbCrO_4$-$R_{V_{Cr}}$) for solar water oxidation, a two-fold increased water oxidation photocurrent was produced on the $PbCrO_4$-$F_{V_{Cr}}$ film photoanodes (1.13 mA cm^{-2} at 1.23 V *vs.* RHE). Meanwhile, faster water oxidation kinetics were achieved on the $PbCrO_4$-$R_{V_{Cr}}$ film photoanodes. The $PbCrO_4$-$F_{V_{Cr}}$ film photoanodes had a water oxidation rate constant (k_{O_2}) of 40.6 s^{-1}, which is ~5 times the k_{O_2} of the $PbCrO_4$-$R_{V_{Cr}}$ film photoanodes (8.2 s^{-1}). Based on experimental and theoretical investigations, $PbCrO_4$ films with fewer Cr defects having higher activity can be ascribed to the following reasons: (i) the presence of Cr defects can result in the formation of a deep energy level in $PbCrO_4$, which is unfavorable to carrier transfer in the bulk of $PbCrO_4$ films; (ii) the presence of Cr defects can cause the formation of unsaturated O dangling bonds on $PbCrO_4$, which are harmful traps for carrier separation on the surface of $PbCrO_4$ films; (iii) Cr has a half-filled $3d^5$ orbital to provide active sites for reaction, so the presence of Cr defects weakens the catalytic activity of $PbCrO_4$ for water oxidation, and the dehydrogenation of *OH into *O becomes the rate-limiting step, which requires a high energy barrier of 1.88 eV.

2 Experimental section

2.1 Preparation of $PbCrO_4$-$F_{V_{Cr}}$ and $PbCrO_4$-$R_{V_{Cr}}$ films

The $PbCrO_4$-$F_{V_{Cr}}$ and $PbCrO_4$-$R_{V_{Cr}}$ films were prepared by drop-coating combined with thermal treatment (Fig. 1). Typically, $Pb(NO_3)_2$ (AR, Aladdin) and $Cr(NO_3)_3$ (AR, Aladdin) were dissolved in 5 mL of distilled water to form 0.2 M Pb^{2+} and 0.2 M Cr^{3+} precursor solutions, respectively. Then, 100 mg of polyethylene glycol (AR, Aladdin) was added to the Pb^{2+} precursor solution to stabilize Pb^{2+}, while 70 μL of acetylacetone (Aladdin, 99.8%) was dropped into the Cr^{3+} precursor solution to stabilize Cr^{3+}. After that, the Pb^{2+} and Cr^{3+} precursor solutions were treated by ultrasonication at 60 °C for 30 min. Subsequently, the Pb^{2+} and Cr^{3+} precursor solutions were mixed and diluted using ethylene glycol (AR, Kelong) to form a 0.01 M Pb^{2+}/Cr^{3+} precursor solution. Finally, 200 μL of Pb^{2+}/Cr^{3+} precursor solution was dropped onto a clean FTO glass (10 × 20 × 2 mm, 15 Ω sq^{-1}), and thermally treated in a muffle furnace (chamber: 20 × 30 × 20 cm) at 500 °C (heating rate: 2.5 °C min^{-1}) for 2 h in air. For the preparation of $PbCrO_4$-$F_{V_{Cr}}$ films, a culture dish (diameter: 6.0 cm; height: 1.6 cm) was used to cover the Pb^{2+}/Cr^{3+} precursor solution during thermal treatment. For comparison, $PbCrO_4$-$R_{V_{Cr}}$ films were prepared without using a culture dish cover during thermal treatment of the Pb^{2+}/Cr^{3+} precursor solution.

To check the presence and content difference of O dangling bonds in the as-prepared $PbCrO_4$ films, $PbCrO_4$-$F_{V_{Cr}}$ and $PbCrO_4$-$R_{V_{Cr}}$ films were immersed in 0.01 M 1-octadecanethiol ($C_{18}H_{38}S$, 97%, Macklin) ethanol solution for 24 h to passivate their O dangling bonds. Then, the two types of $PbCrO_4$ film were washed with deionized water for photocurrent measurements.

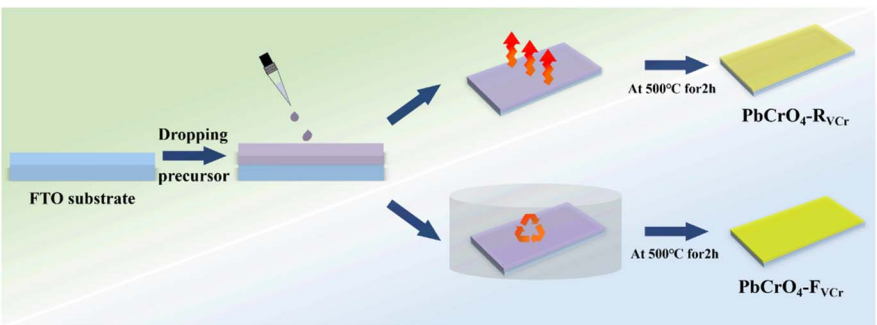

Fig. 1 Diagram of $PbCrO_4$-$F_{V_{Cr}}$ and $PbCrO_4$-$R_{V_{Cr}}$ film preparation.

2.2 Characterizations of samples

The crystal structure, morphology and elemental chemical state of the $PbCrO_4$-$F_{V_{Cr}}$ and $PbCrO_4$-$R_{V_{Cr}}$ films were characterized using an X-ray diffraction (XRD, SmartLab-9 kW, Rigaku), scanning electron microscopy (SEM, Regulus 8100), transmission electron microscopy (TEM, Tecnai G220) and X-ray photoelectron spectroscopy (XPS, ESCALAB 250Xi), respectively. The UV-vis absorption spectra for the $PbCrO_4$-$F_{V_{Cr}}$ and $PbCrO_4$-$R_{V_{Cr}}$ films were measured using a Hitachi spectrophotometer (UH5700). The photoluminescence emission (PL) spectra for the $PbCrO_4$-$F_{V_{Cr}}$ and $PbCrO_4$-$R_{V_{Cr}}$ films were recorded using an FLS1000 photoluminescence spectrometer. The electron paramagnetic resonance (EPR) spectra for the $PbCrO_4$-$F_{V_{Cr}}$ and $PbCrO_4$-$R_{V_{Cr}}$ films were recorded using a Bruker EPR spectrometer (EMPplus-10/12). The water contact angle of the $PbCrO_4$-$F_{V_{Cr}}$ and $PbCrO_4$-$R_{V_{Cr}}$ films was observed using a contact angle meter (SINDIN, SCD-100). The surface photovoltage and transient surface photovoltage spectra for the $PbCrO_4$-$F_{V_{Cr}}$ and $PbCrO_4$-$R_{V_{Cr}}$ films were detected using surface photovoltage spectroscopy (Beijing China Education Au-light Co., Ltd, CEL-TPV2000). For the $PbCrO_4$-$F_{V_{Cr}}$ and $PbCrO_4$-$R_{V_{Cr}}$ films before and after stability testing, their Raman spectra were detected using a Raman spectrometer (MultiRAM, Bruker).

2.3 Photoelectrochemical measurements

All PEC measurements were conducted on a CHI 760e electrochemical workstation with a three-electrode cell at room temperature. The as-prepared $PbCrO_4$ films were used directly as working electrodes; the counter electrode was a Pt wire (99%), and the reference electrode was an Ag/AgCl electrode. The light source was a 300 W xenon lamp (Beijing China Education Au-light Co., Ltd) equipped with a 1.5G filter to provide 100 mW cm^{-2} illumination. The PEC measurements were carried out using back-side illumination, namely the light first penetrated the FTO, then the $PbCrO_4$ film. 0.5 M phosphate buffer (PBS, pH 7.0) aqueous solution and 0.1 M potassium hydrogen phthalate (KHP)/0.5 M Na_2SO_3 mixed aqueous solution were used as the electrolytes. The potential applied on the working electrode was converted into RHE potential using the following equation:

$$E_{RHE} = E_{Ag/AgCl} + 0.0592\ pH + 0.197 \quad (1)$$

where $E_{Ag/AgCl}$ is the applied potential, and pH is the pH of the electrolyte.

The charge separation (η_{sep}) and injection (η_{inj}) efficiency testing were performed in 0.5 M PBS/0.2 vol% H_2O_2 electrolyte. The η_{sep} and η_{inj} of the $PbCrO_4$-$F_{V_{Cr}}$ and $PbCrO_4$-$R_{V_{Cr}}$ film photoanodes were calculated according to the following equations:

$$\eta_{sep} = \frac{J_{H_2O_2}}{J_{abs}} \times 100\% \quad (2)$$

$$\eta_{inj} = \frac{J}{J_{H_2O_2}} \times 100\% \quad (3)$$

where J_{abs} is the calculated photocurrent density based on the UV-vis absorption data of the films (Fig. 6a), $J_{H_2O_2}$ is the photocurrent density of the film photoanodes in 0.5 M PBS/0.2 vol% H_2O_2 (Fig. S5), and J is the photocurrent density of the film photoanodes in 0.5 M PBS.

The applied bias photon-to-current efficiency (ABPE) of the $PbCrO_4$-$F_{V_{Cr}}$ and $PbCrO_4$-$R_{V_{Cr}}$ film photoanodes was calculated using the following equation:

$$ABPE = \frac{j(mA\ cm^{-2}) \times (1.23 - E_{RHE})}{100\ mW\ cm^{-2}} \times 100\% \quad (4)$$

where E_{RHE} is the applied potential *vs.* RHE and j is the photocurrent density of the film photoanodes under AM 1.5G illumination.

The Mott–Schottky plots of $PbCrO_4$-$F_{V_{Cr}}$ and $PbCrO_4$-$R_{V_{Cr}}$ film photoanodes were recorded in the potential range of 0.3 to 0.5 V *vs.* RHE under AM 1.5G illumination. The carrier concentration of the $PbCrO_4$-$F_{V_{Cr}}$ and $PbCrO_4$-$R_{V_{Cr}}$ films was calculated using the following equation:

$$1/C^2 = (2/e\varepsilon\varepsilon_0 A^2 N_d)(V_a - V_{fb} - kT/e) \quad (5)$$

where C is the capacitance, ε is the relative dielectric constant of $PbCrO_4$, ε_0 is the permittivity of vacuum (8.854×10^{-12} F cm^{-1}), k is the Boltzmann constant (1.381×10^{-23} J K^{-1}), e is the elemental charge (1.602×10^{-19} C), A is the surface area of the sample, N_d is the carrier concentration, V_a is the applied potential, V_{fb} is the flat band potential, and T is temperature.

The electrochemical impedance spectroscopy (EIS) measurements were performed at 1.23 V *vs.* RHE. The testing frequency ranged from 100 000 to 0.01 Hz with an amplitude of 10 mV. The measured EIS data were fitted by Zview software under the proposed equivalent circuit model. Based on the EIS Bode plots, the hole lifetimes (τ) on the two types of $PbCrO_4$ film photoanode were obtained using the following equation:

$$\tau = \frac{1}{2}\pi f_m \quad (6)$$

where f_m is the maximum phase in the frequency range.

The water oxidation rate constant (k_{O_2}) and charge transfer rate constant (k_{tran}) of the two types of $PbCrO_4$ film photoanode were calculated on the basis of the fitted components' values for the equivalent circuit (the values shown in Table 2).[18–21] k_{O_2} was calculated through the following equation:

$$k_{O_2} = \frac{1}{R_{ct}CPE_{ct}} \quad (7)$$

k_{tran} was calculated by the following equation:

$$k_{tran} = \frac{1}{R_{sc}CPE_{sc}} \quad (8)$$

where R_{ct} is the water oxidation resistance, R_{sc} is the charge transfer resistance, CPE_{ct} is the constant phase element of electrolyte/photoelectrode, and CPE_{sc} is the constant phase element of the photoelectrode surface.

2.4 Density functional theory calculations

The charge density and the density of states of $PbCrO_4$ (120) with and without Cr defects were calculated using the Vienna *Ab*

initio Simulation Package (VASP).[22,23] The exchange–correlation potential was described by the Perdew–Burke–Ernzerhof (PBE) generalized gradient approach (GGA).[24] The electron–ion interactions were accounted for by the projector augmented wave (PAW) model.[25] All density functional theory (DFT) calculations were performed with a cut-off energy of 400 eV, and the Brillouin zone was sampled using a 2 × 1 × 1 Gamma-centered *k*-point Monkhorst–Pack grid. The energy and force convergence criteria of the self-consistent iteration were set to 10^{-4} eV and 0.05 eV $Å^{-1}$, respectively. The DFT-D3 method was used to describe van der Waals (vdW) interactions.[26]

The Gibbs free energy changes (ΔG) of water oxidation on $PbCrO_4$ (120) with and without Cr defects were calculated using the following formula:

$$\Delta G = \Delta E + \Delta \mathrm{ZPE} - T\Delta S + \Delta G_{\mathrm{U}} + \Delta G\mathrm{pH} \quad (9)$$

where ΔE is the difference in electron energies calculated by DFT; ΔZPE and ΔS are the changes of zero-point energy and entropy, respectively, which are obtained from vibrational frequencies. T is the temperature (298.15 K). $\Delta G_{\mathrm{U}} = -eU$, where U is the applied electrode potential. $\Delta G_{\mathrm{pH}} = k_{\mathrm{B}}T \times \ln 10 \times \mathrm{pH}$, where k_{B} is the Boltzmann constant.

3 Results and discussion

3.1 Characterization results

Fig. 2a–f show the typical SEM images of $PbCrO_4$-$R_{V_{Cr}}$ and $PbCrO_4$-$F_{V_{Cr}}$ films. From the top and sectional SEM images shown in Fig. 2a–c, it can be seen that $PbCrO_4$-$R_{V_{Cr}}$ films are not dense and flat enough, and obvious gaps are formed and evenly distributed throughout the whole film. By comparison, $PbCrO_4$-$F_{V_{Cr}}$ films were denser and flatter, with few gaps (Fig. 2d–f). In terms of microscopic morphology, $PbCrO_4$-$R_{V_{Cr}}$ and $PbCrO_4$-$F_{V_{Cr}}$ films consist of connected nanoparticles, but the nanoparticle size of $PbCrO_4$-$R_{V_{Cr}}$ films (average size ~70 nm) was smaller than that of $PbCrO_4$-$F_{V_{Cr}}$ films (average size ~100 nm) (Fig. 2b, e and S1 in SI). In general, $PbCrO_4$-$R_{V_{Cr}}$ films (~230 nm, Fig. 2c) were slightly thicker than $PbCrO_4$-$F_{V_{Cr}}$ films (~200 nm, Fig. 2f), due to the difference in morphology and evenness, although their preparation used the same amount of Pb^{2+}/Cr^{3+} precursor solution. In the HRTEM image of the $PbCrO_4$-$F_{V_{Cr}}$ film, the crystalline feature was observed and the lattice spacing was ~0.32 nm, which corresponds to the typical crystal feature of $PbCrO_4$(120) (Fig. 2g). For the preparation of the two types of $PbCrO_4$ films, the only condition difference was the presence or absence of a culture dish covering the Pb^{2+}/Cr^{3+} precursor solution during annealing treatment. During the evaporation and pyrolysis of the Pb^{2+}/Cr^{3+} precursor solution, the use of a culture dish cover enabled the precursor solution to gradually convert into a uniform colloid and film, in contrast to the process without a cover (Fig. S2). The morphology and thickness differences between the $PbCrO_4$-$R_{V_{Cr}}$ and $PbCrO_4$-$F_{V_{Cr}}$ films suggested that the formation of the $PbCrO_4$ film was significantly impacted by the culture dish covering above the Pb^{2+}/Cr^{3+} precursor solution during thermal treatment. In further XRD analyses, the typical diffraction peaks of monoclinic $PbCrO_4$ (PDF#: 08-0209) were clearly observed for both types of $PbCrO_4$

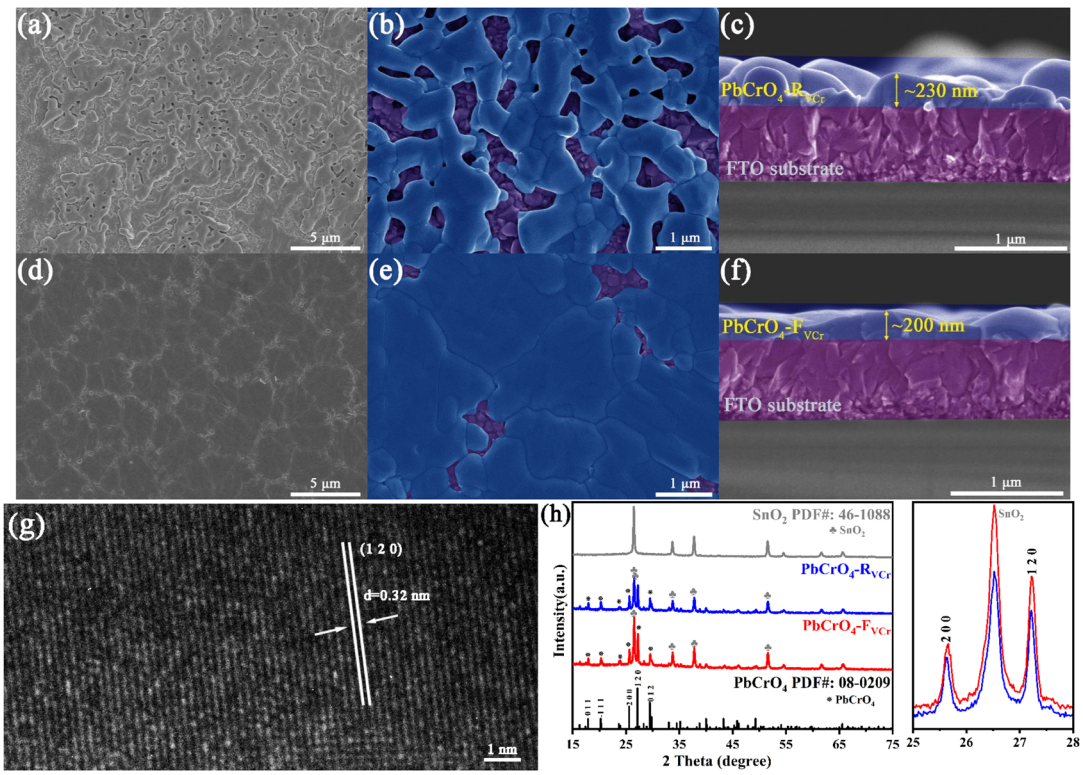

Fig. 2 SEM images of (a–c) $PbCrO_4$-$R_{V_{Cr}}$ and (d–f) $PbCrO_4$-$F_{V_{Cr}}$ films. (g) HRTEM image of $PbCrO_4$-$F_{V_{Cr}}$ film. (h) XRD patterns for $PbCrO_4$-$R_{V_{Cr}}$ and $PbCrO_4$-$F_{V_{Cr}}$ films.

Table 1 The crystallinity of $PbCrO_4$-$R_{V_{Cr}}$ and $PbCrO_4$-$F_{V_{Cr}}$ films

Sample	*hkl*	2Θ	FWHM	Crystallinity (%)
$PbCrO_4$-$F_{V_{Cr}}$ film	(200)	25.636	0.156	85.58
	(120)	27.223	0.133	
$PbCrO_4$-$R_{V_{Cr}}$ film	(200)	25.624	0.118	80.41
	(120)	27.218	0.107	

film, in addition to the signals for the FTO substrate (SnO_2, PDF#:46-1088) (Fig. 2h). Significantly, the (120) diffraction peak intensity of the $PbCrO_4$-$F_{V_{Cr}}$ film was 1.26 times that of the $PbCrO_4$-$R_{V_{Cr}}$ film. According to the XRD data, the crystallinity of the $PbCrO_4$-$F_{V_{Cr}}$ film was found to be 85.58%, which is higher than that of the $PbCrO_4$-$R_{V_{Cr}}$ film (80.41%) (Table 1). It is generally believed that the crystallinity of metal oxides is closely influenced by the defect content.[15] The crystallinity difference implied that the defect content in the $PbCrO_4$-$R_{V_{Cr}}$ and $PbCrO_4$-$F_{V_{Cr}}$ films is different.

To determine the chemical states of the constituent elements, the $PbCrO_4$-$R_{V_{Cr}}$ and $PbCrO_4$-$F_{V_{Cr}}$ films were further investigated using XPS. In the survey spectra, the XPS signals of O 1s, Pb 4f and Cr 2p were clearly detected on the $PbCrO_4$-$R_{V_{Cr}}$ and $PbCrO_4$-$F_{V_{Cr}}$ films (Fig. S3). In the high-resolution Pb 4f spectrum of both types of $PbCrO_4$ film, the binding energy peaks at 138.27 and 143.12 eV were in good agreement with the Pb^{2+} in monoclinic $PbCrO_4$ (Fig. 3a).[27,28] For the high-resolution Cr 2p spectrum, the binding energy peaks of the $PbCrO_4$-$R_{V_{Cr}}$ and $PbCrO_4$-$F_{V_{Cr}}$ films generally matched the Cr 2p signals in monoclinic $PbCrO_4$ (Fig. 3b).[29,30] However, the Cr 2p binding energy peaks of $PbCrO_4$-$R_{V_{Cr}}$ film (578.67 eV, 587.92 eV) negatively shifted relative to those of the $PbCrO_4$-$F_{V_{Cr}}$ film (578.87 eV, 588.12 eV), hinting that their Cr have slightly different chemical states. Meanwhile, more obvious oxygen vacancy signals were found in the high-resolution O 1s spectrum of the $PbCrO_4$-$R_{V_{Cr}}$ film in comparison with the $PbCrO_4$-$F_{V_{Cr}}$ film, in addition to their similar lattice oxygen and adsorbed oxygen signals (Fig. 3c). Taking into account the Cr 2p and O 1s XPS differences between the $PbCrO_4$-$R_{V_{Cr}}$ and $PbCrO_4$-$F_{V_{Cr}}$ films, it can be inferred that the $PbCrO_4$-$R_{V_{Cr}}$ film contains more defects than the $PbCrO_4$-$F_{V_{Cr}}$ film. To detect the specific defects in $PbCrO_4$-$R_{V_{Cr}}$ and $PbCrO_4$-$F_{V_{Cr}}$ films, their EPR spectra were recorded and compared. As shown in Fig. 3d–f, two signal centers at $g = 2.003$ and $g = 3.883$ appeared for both types of $PbCrO_4$ film, which are the typical EPR signals of oxygen vacancies and Cr defects, respectively.[31–34] In comparison, the EPR signals of Cr defects were much stronger than those of oxygen vacancies, indicating that Cr defects are the predominant defects in $PbCrO_4$-$R_{V_{Cr}}$ and $PbCrO_4$-$F_{V_{Cr}}$ films and oxygen vacancies are companion species. Obviously, the $PbCrO_4$-$R_{V_{Cr}}$ film had stronger Cr defects and oxygen vacancy signals than the $PbCrO_4$-$F_{V_{Cr}}$ film, indicating a higher content of Cr defects in the $PbCrO_4$-$R_{V_{Cr}}$ film. For the preparation of both types of $PbCrO_4$ film, the only condition difference was the presence and absence of a culture dish covering above the Pb^{2+}/Cr^{3+} precursor solution during the annealing treatment. The above characterizations show that $PbCrO_4$ films with few Cr defects can be prepared using a culture dish covering above the Pb^{2+}/Cr^{3+} precursor solution to reduce the loss of Cr during thermal treatment.

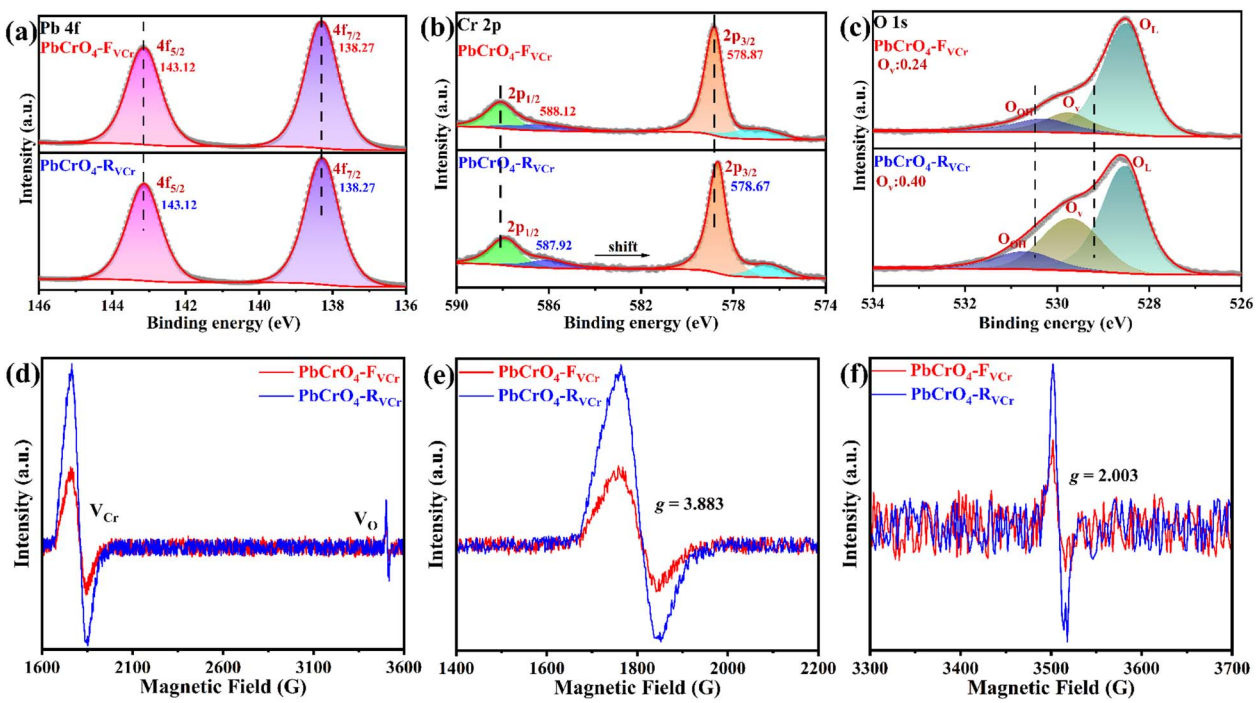

Fig. 3 High-resolution XPS spectra for (a) Pb 4f, (b) Cr 2p and (c) O 1s of $PbCrO_4$-$R_{V_{Cr}}$ and $PbCrO_4$-$F_{V_{Cr}}$ films. (d–f) EPR spectra for $PbCrO_4$-$R_{V_{Cr}}$ and $PbCrO_4$-$F_{V_{Cr}}$ films.

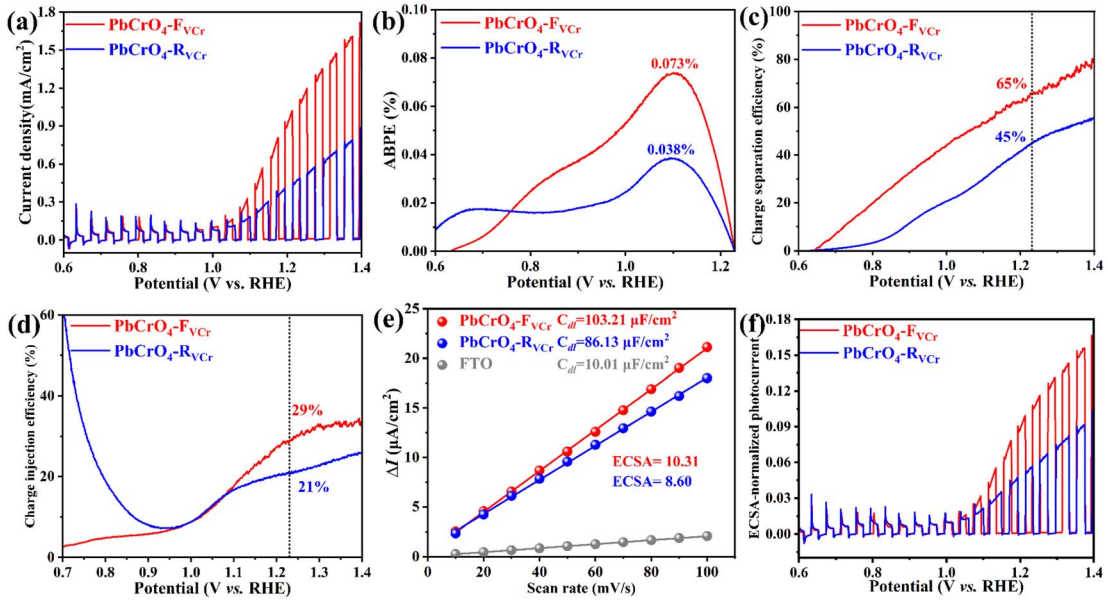

Fig. 4 (a) Chopped LSV curves, (b) ABPE, (c) η_{sep}, (d) η_{inj}, (e) ECSA, and (f) ECSA-normalized photocurrent for $PbCrO_4$-$R_{V_{Cr}}$ and $PbCrO_4$-$F_{V_{Cr}}$ film photoanodes in 0.5 M PBS.

3.2 $PbCrO_4$-$R_{V_{Cr}}$ and $PbCrO_4$-$F_{V_{Cr}}$ films as photoanodes for solar water oxidation

In previous reports, $PbCrO_4$ films have been demonstrated to work as photoanodes for solar water oxidation in PBS solution, and their activity can be directly reflected in the magnitude of the photocurrent.[4,6] To check the influence of Cr defects on the solar water oxidation activity of $PbCrO_4$ photoanodes, the photocurrent of the two types of $PbCrO_4$ film was measured in 0.5 M PBS under AM 1.5G irradiation. As shown in Fig. 4a and S4, a higher photocurrent is produced on the $PbCrO_4$-$F_{V_{Cr}}$ film than on the $PbCrO_4$-$R_{V_{Cr}}$ film. At 1.23 V *vs.* RHE, the $PbCrO_4$-$F_{V_{Cr}}$ film had a higher photocurrent of 1.13 mA cm^{-2} compared to the $PbCrO_4$-$R_{V_{Cr}}$ film (0.55 mA cm^{-2}), indicating its higher solar water oxidation activity. In ABPE measurement, the higher activity was further observed on the $PbCrO_4$-$F_{V_{Cr}}$ film photoanode; their maximum ABPE (0.073%) was nearly double that of the $PbCrO_4$-$R_{V_{Cr}}$ film photoanode (0.038%) (Fig. 4b). It is important to note that the $PbCrO_4$-$F_{V_{Cr}}$ film in the present work has impressive activity compared with recently reported $PbCrO_4$ films (Table S1). In η_{sep} detection, $PbCrO_4$-$F_{V_{Cr}}$ and $PbCrO_4$-$R_{V_{Cr}}$ film photoanodes were found to have η_{sep} of 65% and 45% at 1.23 V *vs.* RHE, respectively (Fig. 4c). Meanwhile, the η_{inj} of $PbCrO_4$-$F_{V_{Cr}}$ and $PbCrO_4$-$R_{V_{Cr}}$ film photoanodes were 29% and 21% at 1.23 V *vs.* RHE, respectively (Fig. 4d). Taking the η_{sep} and η_{inj} differences between the two types of $PbCrO_4$ film photoanodes as comparisons, it can be found that the $PbCrO_4$-$F_{V_{Cr}}$ and $PbCrO_4$-$R_{V_{Cr}}$ film photoanodes exhibit a more significant difference in charge separation than in charge injection. The η_{sep} and η_{inj} results suggested that $PbCrO_4$ films with fewer Cr defects can achieve charge separation more effectively.[35] From the morphology observations shown in Fig. 2a–f, the $PbCrO_4$-$R_{V_{Cr}}$ film appears to have a larger specific surface area than the $PbCrO_4$-$F_{V_{Cr}}$ film, due to the presence of more gaps. However, electrochemically active surface area (ECSA) testing showed that the $PbCrO_4$-$F_{V_{Cr}}$ films have a larger ECSA (10.31) than the $PbCrO_4$-$R_{V_{Cr}}$ film (8.60) (Fig. 4e and S6). In addition, higher electrochemical water oxidation activity was observed on the $PbCrO_4$-$F_{V_{Cr}}$ film than on the $PbCrO_4$-$R_{V_{Cr}}$ film under dark conditions (Fig. S7). In terms of the electron configuration of transition metal electrocatalysts,[36] Cr would have higher catalytic activity for water splitting than Pb, since Cr has a half-filled 3d orbital ($1s^2 2s^2 2p^6 3s^2 3p^6 3d^5 4s^1$) to provide active sites for reaction, while Pb has a full-filled 3d and 5d orbitals ($1s^2 2s^2 2p^6 3s^2 3p^6 4s^2 3d^{10} 4p^6 5s^2 4d^{10} 5p^6 6s^2 4f^{14} 5d^{10} 6p^2$).[37] Therefore, it can be understood that $PbCrO_4$ with more Cr defects has lower electrochemical activity for water oxidation. Based on the photocurrent and ECSA data, it was found that the $PbCrO_4$-$F_{V_{Cr}}$ film has a higher ECSA-normalized photocurrent than the $PbCrO_4$-$R_{V_{Cr}}$ film (Fig. 4f). The above findings jointly demonstrate that $PbCrO_4$ films with fewer Cr defects can work as higher activity photoanodes for solar water splitting.

To get insight into the water oxidation kinetics on the two types of $PbCrO_4$ film photoanode, their Nyquist and Bode plots were recorded at 1.23 V *vs.* RHE in 0.5 M PBS under AM 1.5G irradiation. As displayed in Fig. 5a, the Nyquist plot of the $PbCrO_4$-$F_{V_{Cr}}$ film photoanode had a smaller arc than that of the $PbCrO_4$-$R_{V_{Cr}}$ film photoanode, suggesting faster kinetics in solar water oxidation. Data fitting indicated that the charge transfer (R_{sc}) and water oxidation (R_{ct}) resistance on the $PbCrO_4$-$F_{V_{Cr}}$ film photoanode were 290 Ω and 186 Ω, respectively (Table 2).[38,39] By comparison, the $PbCrO_4$-$R_{V_{Cr}}$ film photoanode had higher R_{sc} (1253 Ω) and R_{ct} (962 Ω). Based on the fitted components' equivalent circuit values, the $PbCrO_4$-$F_{V_{Cr}}$ film photoanode was found to have higher k_{O_2} and k_{tran} (k_{O_2}: 40.6 s^{-1}; k_{tran}: 63.3 s^{-1}) than the $PbCrO_4$-$R_{V_{Cr}}$ film photoanode (k_{O_2}: 8.2 s^{-1}; k_{tran}: 40.6 s^{-1}) (Fig. 5b), indicating faster water oxidation and charge transfer rates on the $PbCrO_4$-$F_{V_{Cr}}$ film photoanode. According to

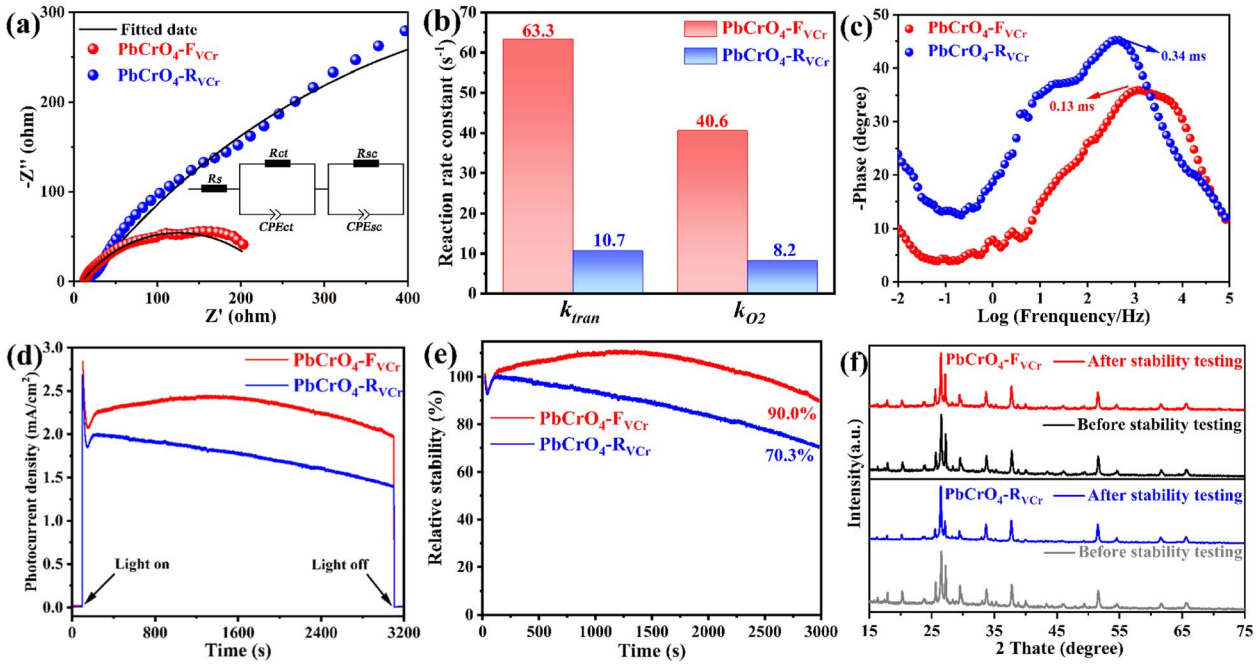

Fig. 5 (a) Nyquist plots, (b) reaction rate constants, and (c) Bode plots for $PbCrO_4O_4$-$R_{V_{Cr}}$ and $PbCrO_4$-$F_{V_{Cr}}$ film photoanodes in 0.5 M PBS at 1.23 V *vs.* RHE under AM 1.5G irradiation. (d) *j*–*t* curves and (e) photocurrent change rate of $PbCrO_4O_4$-$R_{V_{Cr}}$ and $PbCrO_4$-$F_{V_{Cr}}$ film photoanodes in 0.1 M KHP/0.05 M Na_2SO_3 at 1.23 V *vs.* RHE under AM 1.5G irradiation. (f) XRD patterns of $PbCrO_4O_4$-$R_{V_{Cr}}$ and $PbCrO_4$-$F_{V_{Cr}}$ films before and after stability testing.

Table 2 Fitted component values for the equivalent circuit of two types of $PbCrO_4$ film photoanodes (inset of Fig. 5a)

Sample	R_s/Ω (error)	R_{ct}/Ω (error)	CPE_{ct}/F (error)	R_{sc}/Ω (error)	CPE_{sc}/F (error)
$PbCrO_4$-$R_{V_{Cr}}$	17.67 (1.98%)	962 (6.26%)	9.72×10^{-5} (5.15%)	1253 (4.39%)	1.50×10^{-4} (7.20%)
$PbCrO_4$-$F_{V_{Cr}}$	10.67 (1.42%)	186 (2.62%)	8.47×10^{-5} (5.23%)	290 (7.93%)	2.80×10^{-4} (7.62%)

the Bode plots, the hole lifetimes (τ) on the $PbCrO_4$-$F_{V_{Cr}}$ and $PbCrO_4$-$R_{V_{Cr}}$ film photoanodes were calculated to be 0.13 ms and 0.34 ms, respectively (Fig. 5c). These outcomes confirmed that the holes on the $PbCrO_4$-$F_{V_{Cr}}$ film photoanode can react with H_2O molecules quickly.[40,41] As previously analyzed, Cr has a half-filled 3d orbital that could provide active sites for water oxidation. Therefore, it is not surprising that the $PbCrO_4$ film photoanode with fewer Cr defects is kinetically favorable for solar water oxidation.

In terms of the stability for solar water oxidation, it was unfortunate that unsatisfactory activity decay was observed on the $PbCrO_4$-$F_{V_{Cr}}$ and $PbCrO_4$-$R_{V_{Cr}}$ film photoanodes in 0.5 M PBS during continuous testing at 1.23 V *vs.* RHE (Fig. S8). Further investigations found that dissolution and photocorrosion issues are the main causes of activity decay on both types of $PbCrO_4$ film photoanode in 0.5 M PBS (please see the result discussions for Fig. S9 to S11 and Table S2 in the SI). According to these findings, the PEC stability testing for the $PbCrO_4$-$F_{V_{Cr}}$ and $PbCrO_4$-$R_{V_{Cr}}$ films was conducted in 0.1 M KHP/0.05 M Na_2SO_3 aqueous solution at 1.23 V *vs.* RHE. As shown in Fig. 5d and e, the $PbCrO_4$-$F_{V_{Cr}}$ film has a higher photocurrent than the $PbCrO_4$-$R_{V_{Cr}}$ film, showing its higher activity for SO_3^{2-} oxidation. After 3000 s of continuous reaction, 90.0% activity was retained on the $PbCrO_4$-$F_{V_{Cr}}$ film, while the $PbCrO_4$-$R_{V_{Cr}}$ film was 70.3% (Fig. 5e). Contrastive XRD, Raman and SEM investigations indicated that the crystalline phases, molecular structure and morphology of the two types of $PbCrO_4$ film photoanode show slight changes after stability testing (Fig. 5f, S10 and S11). However, the $PbCrO_4$-$R_{V_{Cr}}$ film after stability testing had a more pronounced decrease in the XRD peaks' intensity, relative to the $PbCrO_4$-$F_{V_{Cr}}$ film (Fig. 5f). From the stability difference between the $PbCrO_4$-$F_{V_{Cr}}$ and $PbCrO_4$-$R_{V_{Cr}}$ film photoanodes, it can be seen that $PbCrO_4$ with fewer Cr defects is more stable to drive PEC reactions.

3.3 The mechanism for the higher activity of $PbCrO_4$ films with fewer Cr defects

The above investigations demonstrated that $PbCrO_4$ films with fewer Cr defects have higher solar water oxidation activity. To reveal the mechanism for $PbCrO_4$ films with fewer Cr defects having higher activity, the physicochemical properties of the $PbCrO_4$-$F_{V_{Cr}}$ and $PbCrO_4$-$R_{V_{Cr}}$ films involving solar water oxidation were contrastively checked. First of all, the UV-vis light absorption property of the two types of $PbCrO_4$ film was investigated. As shown in Fig. 6a, the $PbCrO_4$-$F_{V_{Cr}}$ and $PbCrO_4$-$R_{V_{Cr}}$ films have a close absorption edge around 550 nm, which

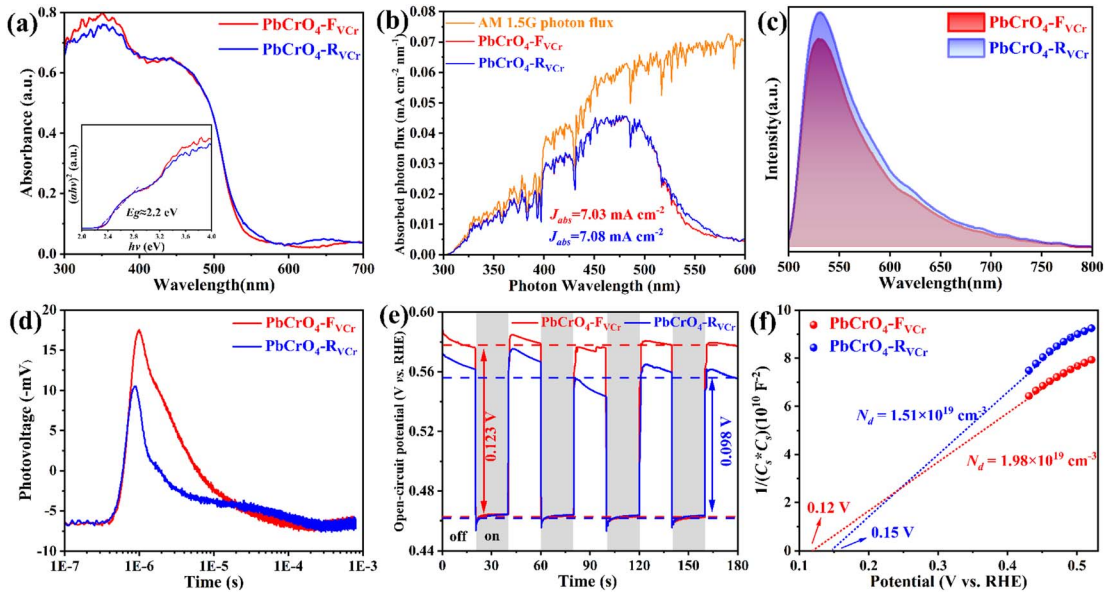

Fig. 6 (a) UV-vis absorption spectra, (b) absorbed photon flux, (c) PL spectra, and (d) transient photovoltage spectra of $PbCrO_4$-$R_{V_{Cr}}$ and $PbCrO_4$-$F_{V_{Cr}}$ films in air. (e) OCP variations and (f) Mott–Schottky plots of $PbCrO_4$-$R_{V_{Cr}}$ and $PbCrO_4$-$F_{V_{Cr}}$ films in 0.5 M PBS under AM 1.5G irradiation.

corresponds to the typical band gap of monoclinic $PbCrO_4$ (~2.2 eV).[1,42] Meanwhile, the light absorption intensity of the two types of $PbCrO_4$ film was very close too, and the absorbed photon fluxes of the $PbCrO_4$-$F_{V_{Cr}}$ and $PbCrO_4$-$R_{V_{Cr}}$ films were 7.03 mA cm^{-2} and 7.08 mA cm^{-2}, respectively (Fig. 6b). These observations indicated that the obvious activity difference between $PbCrO_4$-$F_{V_{Cr}}$ and $PbCrO_4$-$R_{V_{Cr}}$ films is not be caused by a difference in their light absorption properties. In PL spectrum investigations, weaker PL peak intensity was detected on the $PbCrO_4$-$F_{V_{Cr}}$ film compared with the $PbCrO_4$-$R_{V_{Cr}}$ film, reflecting lower carrier recombination in/on the $PbCrO_4$-$F_{V_{Cr}}$ film (Fig. 6c). In addition, stronger surface photovoltage signals were detected on the $PbCrO_4$-$F_{V_{Cr}}$ films than on the $PbCrO_4$-$R_{V_{Cr}}$ film, further confirming better carrier separation and transfer in/on the $PbCrO_4$-$F_{V_{Cr}}$ film (Fig. 6d and S12). As mentioned in the Introduction, the presence of a high concentration of Cr defects in monoclinic $PbCrO_4$ could disrupt its CrO_4 tetrahedron network and form defect-level traps, which are disadvantageous to the delocalized separation and transfer of electrons/holes in theory. To confirm the effect of Cr defects on carrier separation and transfer, the open-circuit potential (OCP) variations were detected on $PbCrO_4$-$F_{V_{Cr}}$ and $PbCrO_4$-$R_{V_{Cr}}$ films under and without AM 1.5G irradiation. As displayed in Fig. 6e, an OCP_{light} of ~0.461 V *vs.* RHE was observed on both types of $PbCrO_4$ film, while the OCP_{dark} of the $PbCrO_4$-$F_{V_{Cr}}$ and $PbCrO_4$-$R_{V_{Cr}}$ films are 0.582 and 0.552 V *vs.* RHE, respectively. Accordingly, a more obvious OCP variation was produced on the $PbCrO_4$-$F_{V_{Cr}}$ film (0.123 V) than the $PbCrO_4$-$R_{V_{Cr}}$ film (0.098 V), suggesting that $PbCrO_4$ films with fewer Cr defects have better charge separation and transfer properties.[43,44] In the Mott–Schottky plots (Fig. 6f), a more negative E_{fb} of 0.12 V *vs.* RHE was observed on the $PbCrO_4$-$F_{V_{Cr}}$ film, relative to the $PbCrO_4$-$R_{V_{Cr}}$ film (0.15 V). Considering the relevance of E_{fb} in n-type semiconductors to their Fermi level position (E_f), the $PbCrO_4$-$F_{V_{Cr}}$ film, having a more negative E_{fb}, indicates that $PbCrO_4$ with fewer Cr defects has a higher E_f and carrier concentration ($PbCrO_4$-$F_{V_{Cr}}$ film: 1.98 × 10^{19} cm^{-3}; $PbCrO_4$-$R_{V_{Cr}}$ film: 1.51 × 10^{19} cm^{-3}).

In terms of chargeability, one Cr^{6+} defect carries three effective negative charges (V_{Cr}''') in monoclinic $PbCrO_4$. From a unit cell structural perspective, the presence of Cr defects could cause the formation of unsaturated O dangling bonds on the $PbCrO_4$ surface. To check the presence and content difference of O dangling bonds on the two types of $PbCrO_4$ film, their hydrophilicity was detected and compared (Fig. 7a). Interestingly, weaker hydrophilicity was observed on the $PbCrO_4$-$R_{V_{Cr}}$ film (θ = 35.4°) relative to the $PbCrO_4$-$F_{V_{Cr}}$ film (θ = 10.2°), although the $PbCrO_4$-$R_{V_{Cr}}$ film had a rougher surface (SEM images shown in Fig. 2a–f). In essence, the hydrophilicity of the film depends on the interaction intensity between H_2O molecules and the surface compounds.[45] It has been reported that high concentrations of Al defects in α-Al_2O_3 can result in the reconstitution of unsaturated O dangling bonds and the decrease of surface energy, thereby α-Al_2O_3 with rich Al defects has weaker hydrophilicity than pristine α-Al_2O_3.[46] The hydrophilicity difference suggested that $PbCrO_4$-$F_{V_{Cr}}$ and $PbCrO_4$-$R_{V_{Cr}}$ films have different contents of O dangling bonds on the surface, owing to their different Cr defect contents. The presence of O dangling bonds usually has a negative effect on carrier separation on the surface of semiconductors.[47,48] Through the –SH groups of 1-octadecanethiol passivating the O dangling bonds on $PbCrO_4$ films,[49–51] the photocurrent of the $PbCrO_4$-$R_{V_{Cr}}$ film was found to increase by 62%, but there was only a 24% increase on the $PbCrO_4$-$F_{V_{Cr}}$ film (Fig. 7b and c). The photocurrent enhancement on 1-octadecanethiol-passivated $PbCrO_4$ films confirmed the presence of O dangling bonds and the negative effect of O dangling bonds on carrier separation on

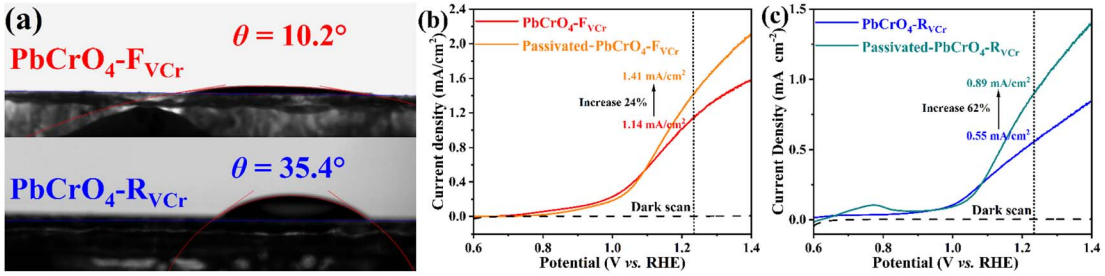

Fig. 7 (a) Water contact angle images of $PbCrO_4$-$F_{V_{Cr}}$ and $PbCrO_4$-$R_{V_{Cr}}$ films. In 0.5 M PBS under AM 1.5G irradiation, LSV curves of (b) $PbCrO_4$-$F_{V_{Cr}}$ and (c) $PbCrO_4$-$R_{V_{Cr}}$ films before and after 1-octadecanethiol passivating.

$PbCrO_4$. Meanwhile, the more obvious photocurrent improvement on the 1-octadecanethiol-passivated $PbCrO_4$-$R_{V_{Cr}}$ film reflected their higher content of O dangling bonds, due to rich Cr defects.

To understand the influence of Cr defects on the band structure and carrier localization of $PbCrO_4$, the density of states and electron localization function of monoclinic $PbCrO_4$ with and without Cr defects were simulated by DFT calculations. As shown in Fig. 8a, $PbCrO_4$ and $PbCrO_4$-V_{Cr} had similar total density of state (TDOS), indicating that their theoretical carrier density is relatively close. From the partial density of state (PDOS) (Fig. 8b and c), the valence and conduction bands of $PbCrO_4$ and $PbCrO_4$-V_{Cr} can be observed to be mainly composed of O 2p and Cr 3d orbitals, respectively. However, two small peaks corresponding to O 2p and Cr 3d orbitals were found at the Fermi level of $PbCrO_4$-V_{Cr} (Fig. 8c), indicating that a deep energy level is formed in the band structure of $PbCrO_4$-V_{Cr} due to the presence of Cr defects. The presence of a deep energy level in $PbCrO_4$ with Cr defects was actually reflected in the surface photovoltage spectrum of $PbCrO_4$-$R_{V_{Cr}}$ films (shown in Fig. 6d), in which small photovoltage trailing in the time scale of 10^{-5}–10^{-4} s was displayed. It has been reported that the formation of a deep energy level in semiconductors usually results in high non-radiative carrier recombination.[52,53] In terms of structural theory, the presence of Cr defects in $PbCrO_4$ could trigger strong non-radiative carrier recombination, as the d–d transition of Cr^{6+} is limited by spin selectivity and its radiation rate is low. Electron localization comparisons suggested that the presence of Cr defects increases the degree of carrier localization in $PbCrO_4$ (Fig. 8d), hinting at the negative impact of Cr defects on carrier transfer in $PbCrO_4$.[54,55] Combined with the experimental findings of higher carrier recombination in/on

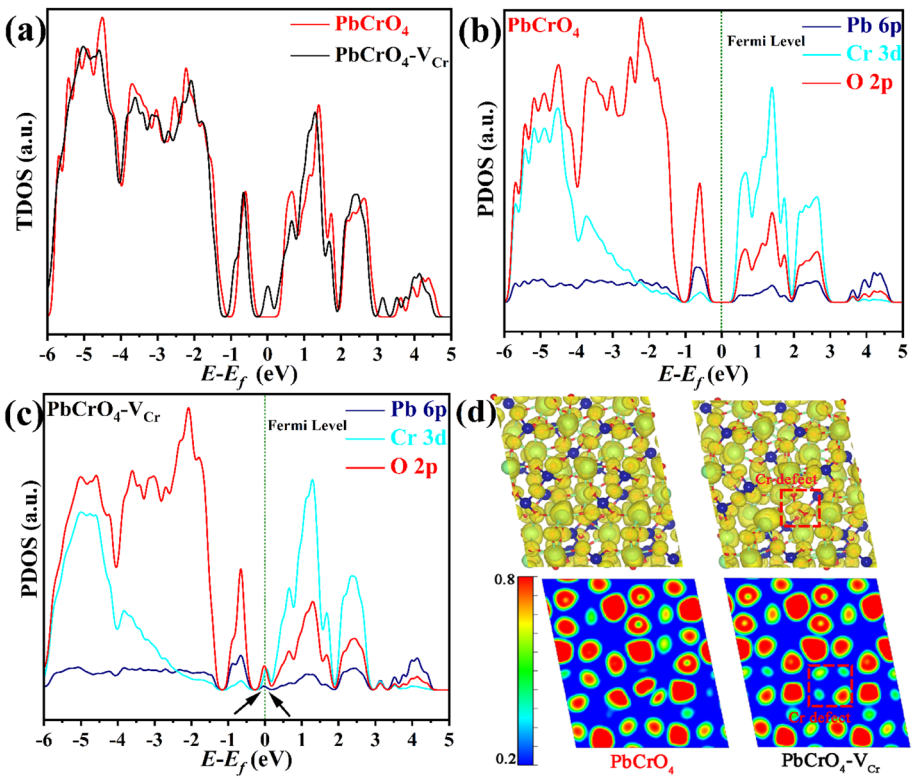

Fig. 8 (a) Total density of states, (b and c) partial density of states, and (d) electron localization function of $PbCrO_4$ with and without Cr defects.

$PbCrO_4$-$R_{V_{Cr}}$ film than $PbCrO_4$-$F_{V_{Cr}}$ film (Fig. 6c and d), it is certain that the presence of Cr defects in $PbCrO_4$ can result in the formation of a deep energy level, which is not conducive to carrier transfer in the bulk of $PbCrO_4$.

The Gibbs free energy (ΔG) of water oxidation on $PbCrO_4$ with and without Cr defects was further simulated by DFT calculations based on a typical four-electron pathway (reactions (1)–(4)).[56,57]

$$H_2O(l) + * \rightarrow *OH + H_2O_2 + H^+ + e^- \quad (1)$$

$$*OH + H_2O(l) + H^+ + e^- \rightarrow *O + H_2O(l) + 2H^+ + 2e^- \quad (2)$$

$$*O + 2H_2O(l) + 2H^+ + 2e^- \rightarrow *OOH + 3H^+ + 3e^- \quad (3)$$

$$*OOH + 3H^+ + 3e^- \rightarrow O_2 + 4H^+ + 4e^- \quad (4)$$

For the adsorption of H_2O on $PbCrO_4$, it was observed that H_2O molecules preferentially adsorbed on the Cr sites of $PbCrO_4$ (Fig. 9a), as Cr has a half-filled 3d orbital to provide active sites.[36] The adsorption energy of H_2O molecules on $PbCrO_4$ was −2.034 eV, which is more negative than that on $PbCrO_4$-V_{Cr} (−1.564 eV). $PbCrO_4$ having a more negative H_2O adsorption energy means that $PbCrO_4$ has better properties for H_2O adsorption than $PbCrO_4$-V_{Cr}, which is consistent with the hydrophilicity results shown in Fig. 7a. For water oxidation, strong H_2O adsorption on photoanodes is energetically favorable for the subsequent dissociation.[58–61] In subsequent calculations for the dehydrogenation of H_2O into O_2 on $PbCrO_4$ and $PbCrO_4$-V_{Cr}, different ΔG values were found in each elementary step (Fig. 9b–d). Significantly, the rate-limiting step of water oxidation on $PbCrO_4$-V_{Cr} was found to be the dehydrogenation of *OH into *O, and its energy barrier was 1.88 eV. For $PbCrO_4$, its rate-limiting step of water oxidation was the reaction of *OH with H_2O to form *OOH, and its energy barrier was 1.61 eV. This comparison indicates that the presence of Cr defects makes the rate-limiting step of water oxidation on $PbCrO_4$ the dehydrogenation of *OH into *O, which has a higher energy barrier of 1.88 eV. Based on the EIS experimental results (Fig. 5a–c and Table 2), it can be further stated that the presence of Cr defects weakens the catalytic activity of $PbCrO_4$ for water oxidation, and turns the rate-limiting step to the dehydrogenation of *OH into *O, which has a high energy barrier of 1.88 eV. Considering the negative effect of Cr defects and the ease of formation of Cr defects in $PbCrO_4$ films using the drop-coating/thermal treatment approach, we discovered that $PbCrO_4$ films with higher water oxidation activity can be prepared using a slightly excess of Cr precursor to compensate for the loss of Cr in thermal treatment, in addition to using a culture dish to cover the precursor solution. As shown in Fig. 9e and f, the highest water oxidation photocurrent was achieved on the $PbCrO_4$ films that

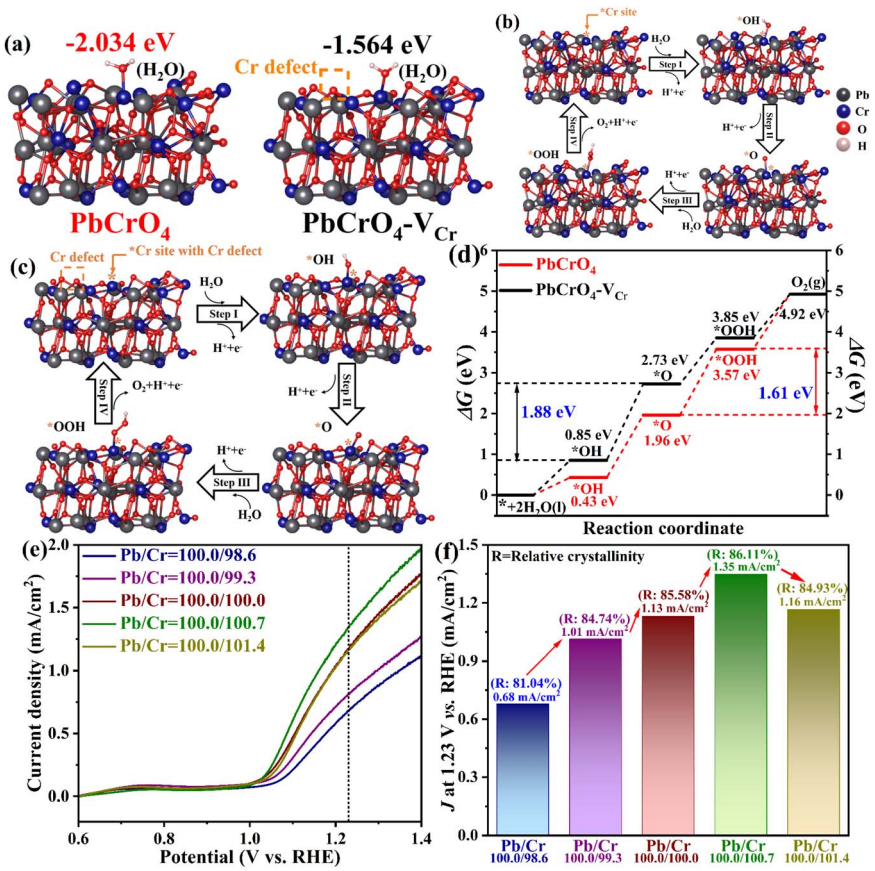

Fig. 9 (a) Adsorption configuration of H_2O on $PbCrO_4$ with and without Cr defects. Intermediate configuration of water oxidation on $PbCrO_4$ (b) with and (c) without Cr defects. (d) Free energy diagrams for water oxidation on $PbCrO_4$ with and without Cr defects at $U = 0$, pH = 0 and $T = 298$ K. (e) LSV curves and (f) water oxidation photocurrent at 1.23 V *vs.* RHE for $PbCrO_4$ films prepared using different Pb/Cr atomic ratios.

were prepared using the precursor solution with a Pb/Cr atomic ratio of 100.0/100.7. Meanwhile, the $PbCrO_4$ film prepared with a Pb/Cr atomic ratio of 100.0/100.7 had the highest crystallinity (86.11%) (Fig. S13 and Table S3). The above findings provide a solution for the preparation of high-activity $PbCrO_4$ films.

Summarizing the findings from experimental observations and DFT calculations, the mechanism for the higher activity of $PbCrO_4$ films with fewer Cr defects can be explained as follows: (i) the presence of Cr defects results in the formation of a deep energy level in $PbCrO_4$, which is unfavorable to carrier transfer in the bulk of $PbCrO_4$ films; (ii) the presence of Cr defects leads to the formation of unsaturated O dangling bonds on $PbCrO_4$, which are harmful traps for carrier separation on the surface of $PbCrO_4$ films; (iii) Cr has a half-filled $3d^5$ orbital to provide active sites for reaction, so the presence of Cr defects weakens the catalytic activity of $PbCrO_4$ for water oxidation, and makes the rate-limiting step the dehydrogenation of *OH into *O, which requires a high energy barrier of 1.88 eV.

4 Conclusions

In summary, monoclinic $PbCrO_4$ films with few Cr defects ($PbCrO_4$-$F_{V_{Cr}}$) were prepared on FTO substrate through drop-coating Pb^{2+}/Cr^{3+} precursor solution to reduce the thermal loss of Cr during annealing treatment. Compared with the monoclinic $PbCrO_4$ film with rich Cr defects ($PbCrO_4$-$R_{V_{Cr}}$), the $PbCrO_4$-$F_{V_{Cr}}$ film as a photoanode had higher solar water oxidation activity. A higher water oxidation photocurrent of 1.13 mA cm^{-2} at 1.23 V *vs.* RHE was produced on the $PbCrO_4$-$F_{V_{Cr}}$ film photoanode, while the $PbCrO_4$-$R_{V_{Cr}}$ film photoanode was 0.55 mA cm^{-2}. Meanwhile, faster water oxidation kinetics were observed on the $PbCrO_4$-$F_{V_{Cr}}$ film photoanode, relative to the $PbCrO_4$-$R_{V_{Cr}}$ film photoanode. The $PbCrO_4$-$F_{V_{Cr}}$ film photoanode had a water oxidation rate constant (k_{O_2}) of 40.6 s^{-1}, and the k_{O_2} of $PbCrO_4$-$R_{V_{Cr}}$ film photoanode was 8.2 s^{-1}. The higher solar water oxidation activity of $PbCrO_4$ films with fewer Cr defects can be attributed to following reasons: (i) the presence of Cr defects can result in the formation of a deep energy level in $PbCrO_4$, which is unfavorable for carrier transfer in the bulk of $PbCrO_4$ films; (ii) the presence of Cr defects can cause the formation of unsaturated O dangling bonds on $PbCrO_4$, which are harmful traps for carrier separation on the surface of $PbCrO_4$ films; (iii) Cr has a half-filled $3d^5$ orbital to provide active sites for reaction, so the presence of Cr defects weakens the catalytic activity of $PbCrO_4$ for water oxidation, and makes the dehydrogenation of *OH into *O the rate-limiting step, which requires a high energy barrier of 1.88 eV. The present work provides insight into monoclinic $PbCrO_4$ film photoanodes in terms of preparation conditions, Cr defects, water oxidation activity and reaction mechanism.

Author contributions

Jiahe Li designed and performed the experiments, and analysed most of the photoelectrochemical data (65%). Gaili Ke analysed partial photoelectrochemical data (35%). Minji Yang assisted with the analysis of DFT calculations data. Guoliang Lv and Lanyi Cao assisted with the XRD and SEM characterizations of samples. Wenjun Li and Wenrong Wang assisted with the XPS and EPR characterizations of samples. Tao Han and Yong Zhou assisted with the preparation and revision of manuscript. Huichao He conceived and directed this work. All authors discussed the results and commented on the manuscript.

Conflicts of interest

The authors declare no competing financial interest.

Data availability

The data supporting this manuscript are available from the corresponding author upon reasonable request.

Supplementary information (SI) is available. See DOI: https://doi.org/10.1039/d5sc08541a.

Acknowledgements

This work was supported by National Natural Science Foundation of China (41702037), Natural Science Foundation of Chongqing (no. CSTB2023NSCQ-MSX0765), and Research Foundation of Chongqing University of Science and Technology (ckrc2022003).

References

1 A. E. Lindberg, W. Wang, S. Zhang, G. Galli and K. S. Choi, *ACS Appl. Energy Mater.*, 2020, **3**, 8658–8666.
2 H. C. Lee, S. K. Cho, H. S. Park, K. M. Nam and A. J. Bard, *J. Phys. Chem. C*, 2017, **121**, 17561–17568.
3 S. K. Cho, R. Akbar, J. Kang, W. Lee and H. S. Park, *J. Mater. Chem. A*, 2018, **6**, 13312–13320.
4 H. Zhou, D. Zhang, X. Gong, Z. Feng, M. Shi, Y. Liu, C. Zhang, P. Luan, P. Zhang, F. Fan, R. Li and C. Li, *Adv. Mater.*, 2022, **34**, 2110610.
5 Y. R. Gwon, J. Kang, S. Choe and S. K. Cho, *J. Electrochem. Soc.*, 2023, **170**, 106504.
6 H. Zhou, D. Zhang, H. Xie, Y. Liu, C. Meng, P. Zhang, F. Fan, R. Li and C. Li, *Adv. Mater.*, 2023, **35**, 2300914.
7 J. Kang, Y. R. Gwon and S. K. Cho, *J. Electroanal. Chem.*, 2020, **878**, 114601.
8 M. G. Walter, E. L. Warren, J. R. McKone, S. W. Boettcher, Q. Mi, E. A. Santori and N. S. Lewis, *Chem. Rev.*, 2010, **110**, 6446–6473.
9 Y. Zhang and J. Yan, *Chem. Eng. J.*, 2023, **472**, 144831.
10 J. Xiong, J. Di, J. Xia, W. Zhu and H. Li, *Adv. Funct. Mater.*, 2018, **28**, 1801983.
11 H. Effenberger and F. Pertlik, *Z. Kristallogr.*, 1986, **176**, 75.
12 D. Errandonea, A. Muñoz, P. Rodríguez-Hernández, J. E. Proctor, F. Sapiña and M. Bettinelli, *Inorg. Chem.*, 2015, **54**, 7524–7535.
13 M. Lamers, S. Fiechter, D. Friedrich, F. F. Abdi and R. van de Krol, *J. Mater. Chem. A*, 2018, **6**, 18694–18700.
14 T. K. van Leeuwen, R. Dowdy, A. Guerrero and P. Gannon, *J. Power Sources*, 2023, **572**, 233065.

15 K. Chen, X. Yuan, Z. Tian, M. Zou, Y. Yuan, Z. Chen, Q. Zhang, Y. Zhang, X. Jin, T. Wu, R. Shahbazian-Yassar and G. Liu, *Nat. Mater.*, 2025, **24**, 835–842.
16 H. Kato, K. Asakura and A. Kudo, *J. Am. Chem. Soc.*, 2003, **125**, 3082–3089.
17 K. Sivula, R. Zboril, F. Le Formal, R. Robert, A. Weidenkaff, J. Tucek, J. Frydrych and M. Grätzel, *J. Am. Chem. Soc.*, 2010, **132**, 7436–7444.
18 J. Xiao, L. Fan, F. Zhao, Z. Huang, S. F. Zhou and G. Zhan, *J. Catal.*, 2020, **381**, 139–149.
19 G. M. Carroll and D. R. Gamelin, *J. Mater. Chem. A*, 2016, **4**, 2986–2994.
20 J. Zhang, R. García-Rodríguez, P. Cameron and S. Eslava, *Energy Environ. Sci.*, 2018, **11**, 2972–2984.
21 C. Debraj, K. Ouchi, Y. Tsubonouchi, Z. N. Zahran and M. Yagi, *Appl. Catal., B*, 2026, **380**, 125733.
22 G. Kresse and J. Hafner, *Phys. Rev. B: Condens. Matter Mater. Phys.*, 1995, **47**, 558.
23 G. Kresse and J. Hafner, *Phys. Rev. B: Condens. Matter Mater. Phys.*, 1994, **49**, 14251.
24 J. P. Perdew, K. Burke and M. Ernzerhof, *Phys. Rev. Lett.*, 1996, **77**, 3865.
25 G. Kresse and D. Joubert, *Phys. Rev. B: Condens. Matter Mater. Phys.*, 1999, **59**, 1758.
26 S. Grimme, J. Antony, S. Ehrlich and H. Krieg, *J. Chem. Phys.*, 2010, **132**, 154104.
27 H. Abdel-Samad and P. R. Watson, *Appl. Surf. Sci.*, 1998, **136**, 46–54.
28 H. Bi, G. Han, M. Guo, C. Ding, H. Zou, Q. Shen, S. Hayase and W. Hou, *ACS Appl. Mater. Interfaces*, 2022, **14**, 35513–35521.
29 M. C. Biesinger, C. Brown, J. R. Mycroft, R. D. Davidson and N. S. McIntyre, *Surf. Interface Anal.*, 2004, **36**, 1550–1563.
30 M. C. Biesinger, B. P. Payne, A. P. Grosvenor, L. W. M. Lau, A. R. Gerson and R. St. C. Smart, *Appl. Surf. Sci.*, 2011, **257**, 2717–2730.
31 L. Wang, S. Zhang, X. Lin, Q. Chen and H. Chen, *Chem. Eng. J.*, 2024, **481**, 147955.
32 D. Zu, Y. Ying, Q. Wei, P. Xiong, M. S. Ahmed, Z. Lin, M. M. Li, M. Li, Z. Xu, G. Chen, L. Bai, S. She, Y. Tsang and H. Huang, *Angew. Chem., Int. Ed.*, 2024, **63**, e202405756.
33 B. Qu and L. Chinese, *J. Lumin.*, 2023, **43**, 1815–1822.
34 F. Gan, H. Deng and H. Liu, *J. Non-Cryst. Solids*, 1982, **52**, 135–141.
35 K. Tsai, C. Lai, Y. Chen, L. Ing-Chi, J. Chang, C. Kuo, S. Tseng, Y. Li and Y. Pu, *Appl. Catal., B*, 2024, **341**, 123288.
36 L. Han, S. Dong and E. Wang, *Adv. Mater.*, 2016, **28**, 9266–9291.
37 J. Chen, H. Li, S. Chen, J. Fei, C. Liu, Z. Yu, K. Shin, Z. Liu, L. Song, H. Graeme, L. Wei and Y. Chen, *Adv. Energy Mater.*, 2021, **11**, 2003412.
38 S. Ye, W. Shi, Y. Liu, D. Li, H. Yin, H. Chi, Y. Luo, N. Ta, F. Fan, X. Wang and C. Li, *J. Am. Chem. Soc.*, 2021, **143**, 12499–12508.
39 W. Nabgan, B. Nabgan, A. A. Jalil, M. Ikram, I. Hussain, M. B. Bahari, T. V. Tran, M. Alhassan, A. H. K. Owgi, L. Parashuram, A. H. Nordin and F. Medina, *Int. J. Hydrogen Energy*, 2024, **52**, 358–380.
40 S. Corby, R. R. Rao, L. Steier and J. R. Durrant, *Nat. Rev. Mater.*, 2021, **6**, 1136–1155.
41 J. Zhang, Y. Deng, D. Gu, S. Wang, L. She, R. Che, Z. S. Wang, B. Tu, S. Xie and D. Zhao, *Adv. Energy Mater.*, 2011, **1**, 241–248.
42 M. Ma, K. Zhang, P. Li, M. S. Jung and M. J. Jeong, *Angew. Chem., Int. Ed.*, 2016, **55**, 11819–11823.
43 K. H. Ye, H. Li, D. Huang, S. Xiao, W. Qiu, M. Li, Y. Hu, W. Mai, H. Ji and S. Yang, *Nat. Commun.*, 2019, **10**, 3687.
44 F. A. L. Laskowski, M. R. Nellist, J. Qiu and S. W. Boettcher, *J. Am. Chem. Soc.*, 2019, **141**, 1394–1405.
45 R. J. Good, *J. Adhes. Sci. Technol.*, 1992, **6**, 1269.
46 K. P. D. Lagerlöf and R. W. Grimes, *Acta Mater.*, 1998, **46**, 5689–5700.
47 H. Wang, S. Jiang, H. Yu, K. Deng, Z. Wang, X. Li, Y. Xu and L. Wang, *J. Mater. Chem. A*, 2023, **11**, 13633–13639.
48 X. Zhong, H. He, M. Yang, G. Ke, Z. Zhao, F. Dong, B. Wang, Y. Chen, X. Shi and Y. Zhou, *J. Mater. Chem. A*, 2018, **6**, 10456–10465.
49 M. Yang, H. He, H. Zhang, G. Ke, X. Zhong, F. Dong, Y. Chen, J. Du and Y. Zhou, *Electrochim. Acta*, 2018, **283**, 871–881.
50 G. Yang, Y. Li, Y. Liu, F. Xie, G. Yan, X. Yang, C. Wei, B. Bian, X. Zhang and N. Lu, *IEEE Trans. Electron Devices*, 2022, **69**, 195–200.
51 X. Min, Q. Xie, Z. Wang, X. Wang and M. Chen, *Mater. Chem. Phys.*, 2022, **276**, 125404.
52 J. Ma, H. Chi, A. Wang, P. Wang, H. Jing and T. Yao, *J. Am. Chem. Soc.*, 2022, **144**, 17540–17548.
53 Z. Zhu, K. Mao, K. Zhang, W. Peng, J. Zhang, H. Meng, S. Cheng, T. Li, H. Lin, Q. Chen, X. Wu and J. Xu, *Joule*, 2022, **6**, 2849–2868.
54 S. Wang, L. Pan, J. Song, W. Mi, J. Zou, L. Wang and X. Zhang, *J. Am. Chem. Soc.*, 2015, **137**, 2975–2983.
55 P. Fuentealba, E. Chamorro, J. Santos and A. Toro-Labbé, *Comput. Theor. Chem.*, 2007, **19**, 57–85.
56 S. Wang, T. He, P. Chen, A. Du, K. Ostrikov, W. Huang and L. Wang, *Adv. Mater.*, 2020, **32**, 2001385.
57 M. Gerosa, F. Gygi, M. Govoni and G. Galli, *Nat. Mater.*, 2018, **17**, 1122–1127.
58 P. Li, X. Chen, H. He, X. Zhou, Y. Zhou and Z. Zou, *Adv. Mater.*, 2018, **30**, 1703119.
59 S. Wan, C. Dong, J. Jin, J. Li, Q. Zhong, K. Zhang and J. H. Park, *ACS Energy Lett.*, 2022, **7**, 3024–3031.
60 P. Yue, H. She, L. Zhang, B. Niu, R. Lian, J. Huang, L. Wang and Q. Wang, *Appl. Catal., B*, 2021, **286**, 119875.
61 X. Wei, J. Zhang, L. Wang, Y. Bai, J. Huang, H. She and Q. Wang, *Chem. Eng. J.*, 2024, **482**, 149114.